Journal of Materials Chemistry A

Accepted Manuscript

ROYAL SOCIETY OF CHEMISTRY

www.rsc.org/materialsA

Journal Name

ARTICLE

3D Hierarchical CuO Mesocrystals from Ionic Liquid Precursor: Towards Better Electrochemical Performance for Li-ion Batteries

Received 00th January 20xx,
Accepted 00th January 20xx

DOI: 10.1039/x0xx00000x

www.rsc.org/

Xiaochuan Duan[a,b,*], Hui Huang[a], Songhua Xiao[a], Jiwei Deng[a,*], Gang Zhou[a], Qiuhong Li[a], and Taihong Wang[a]

CuO mesocrystals have been synthesized by nonclassical crystallization in the presence of ionic liquid and *n*-butylamine under hydrothermal conditions. The resultant mesocrystals are comprised of anisotropic nanosheets and nanorods as building blocks and possess a distinct 3D hierarchical superstructure exposed {001} crystal planes. The mechanisms underlying the sequential formation of the mesocrystals are as follows: amorphous particles first appeared under the high degree of supersaturation by Ostwald rule of stages; then, nanosheet subunits were favored to form due to the protection of {001} planes by *n*-butylamine molecule and etch of {010} planes by hydrolysis reaction, leading to the formation of large number of dangling bonds in the {010} planes. Therefore, ionic liquid can interact with those primary particles to facilitate a self-assembly superstructure by π–π interactions along [010] direction due to high ionic nature, resulting the 3D framework structure of primary particles composed of nanosheet and nanorod subunits by oriented attachment. Moreover, owing to the inherent porosity associated with well-defined nanoparticle orientation, 3D hierarchical CuO mesocrystals achieved a higher electrochemical property as anode for Li-ion battery, surpassing the performance of CuO nanosheets and CuO nanorods. The unique characteristics of hierarchical mesostalline electrodes show an ideal geometry to form stable SEI film, which offers a facile route in designing high-performance electrodes for long-lived Li-ion batteries.

1. Introduction

Motivated by oriented attachment mechanism, the search for mesocrystal, an entirely new class of alternative crystal family with respect to conventional polycrystal and single crystal, has been obtained more and more attentions started in 2005 proposed by Cölfen and Antonietti group.[1] Mesocrystals have since been increasingly investigated in the past decade and become symbols of new and fast developing area of nanotechnology. In particular, mesocrystal can be delineated as crystallographically oriented nanoparticle superstructures with high degree of crystallinity and porosity resulted from non-classical crystallization. The main mesocrystal formation pathways include: ordering by an organic matrix, physical fields or interparticle forces, mineral brides, space constraints. Other formation mechanisms, including topotactic coversion, polyer-mediation or a combination of these meachanisms, can also be observed for mesocrystals[2] To date, a broad range of interesting inorganic mesocrystals have been fabricated, and their morphologies are mainly determined the nanoparticle subunits and the pattern they ordered self-assembly. The nanoparticle subunits (also denoted as primary building blocks) in the most of these mesocrystals are generally nanoparticles of relatively small size with low aspect ratio (less than 50 nm), and there have been rare examples showing the nanoparticle subunits of larger size.[3-9] Moreover, these nanoparticle subunits can achieve crystallographic orientation in mainly one or two preferred direction, leading to the formation of one-dimensional (1D) or two-dimensional (2D) mesocrystals in most of the cases. There is rare work demonstration the synthesis of there-dimensional (3D) mesocrystal with distinct structural and geometrical features such as arrays, networks and hierarchical structures. Therefore, compared to the mesocrystals composed of densely stacked nanoparticles with low aspect ratio, 3D hierarchical mesocrystals assembled by 1D (or 2D) nanoparticle subunits offer more unique characteristics combining both 1D (or 2D) and collective physical properties.[10-13] However, it still remains a great challenge to fabricate hierarchical mesocrystals with low filling factor because of the tendency toward parallel stacking of highly anisotropic shapes.

Another technical difficulty for preparation of 3D hierarchical mesocrystals is challenged by the thermodynamic growth mechanism of crystal: a mesocrystal can easily fuse to a single crystal if the surface of nanoparticle subunits is not sufficiently stabilized, since the nanoparticle subunits are already crystallgraphically aligned so that a crystallographic fusion is thermodynamically favored. To address this issue,

[a] *Pen-Tung Sah Institute of Micro-Nano Science and Technology, Xiamen University, Xiamen, 361005, PR China.*
[b] *College of Chemistry and Chemical Engineering, Xiamen University, Xiamen, 361005, PR China.*
* Corresponding authors: Prof. Xiaochuan Duan E-mail: xcduan@xmu.edu.cn; Prof. Jiwei Deng E-mail: djw@xmu.edu.cn.
Electronic Supplementary Information (ESI) available: [XRD patterns, FT-IR Spectra, and Nyquist plots of CuO samples]. See DOI: 10.1039/x0xx00000x

polymer additives have been necessarily employed to temporarily stabilize (steric or electrosteric stabilization) the nanoparticle subunits and thus prevent the crystallographic fusion of mesocrystals to single crystals.[9, 14-20] Nevertheless, the fabrication of hierarchical mesocrystals directly by nanoparticle subunits programmed hierarchical self-assembly requires face selective polymer adsorption, which is really difficult to realize due to the short-range order and weak selectivity of polymer molecular adsorption. Therefore, reaching higher levels of hierarchical mesocrystals requires further organization of nanoparticle subunits self-assembly that employ long ranging interactions or interparticle forces. In this respect, ionic liquids composed of completely ions can be regarded as promising alternative of conventional organic solvent. Different from typical molecular solvent, ionic liquids have highly ionic nature, the components of ionic liquids (both cation and anion) could strongly interact with the nanoparticle subunits to facilitate a well-defined layered structure at charged surfaces of nanoparticle subunits. Moreover, ionic liquids can form extended hydrogen bond systems in the liquid state and are therefore highly structured. In addition, ionic liquids are referred as "designer solvent" with tunable physicochemical properties and desired functions by changing their components. Thereby, ionic liquids with special cations and anions can be tailored according to composition, initial crystalline structure, and growth habit of the resultant materials. These properties of structural organization make ionic liquids can be used as prospective media for the preparation of hierarchical mesocrystals.[21-29]

As an important transition-metal oxide, copper oxide (CuO) is of particular interest as a promising anode material for lithium-ion batteries owing to its good safety, low toxicity, and large theoretical capacity (670 mAh g^{-1}).[30-41] However, it should be noted that bulk CuO electrodes often suffer from low capacity and poor cycle performance due to their low electrical conductivity, significant volume expansion, and unstable solid electrolyte interface (SEI) film during discharge-charge processes. Taking into account that mesocrystals display inherent porosity associated with well-defined nanoparticle orientation, CuO mesocrystals could be exceedingly beneficial for lithium-ion batteries because of more prevalent pores ease intercalation by decreasing the Li^+ ion diffusion distance and pathways, thus can act as a buffering layer to alleviated the adverse effect of volume expansion experienced during discharge-charge reactions, which can effectively improve the electrochemical performance.[21, 42-57] To this end, we try to introduce this strategy of mesocrystalline modification into CuO electrodes in the present study. By a facile one-pot approach employing ionic liquid precursor that permits control over the morphology and crystal form, 3D hierarchical CuO mesocrystals composed of nanosheet and nanorod subunits can be successfully fabricated without polymer additives in the reaction system. Adjusting the concentration of ionic liquid can also produce other CuO nanostructures with different morphologies, including butterfly-like nanosheets and nanorods. The mechanism for the formation of hierarchical CuO mesocrystals was proposed on the basis of the characterization. Our results demonstrate the ionic liquid (1-*n*-butyl-3-methylimidazolium chloride, [Bmim]Cl) plays a key role on forming CuO nanostructures with different morphologies and crystal forms, thus leading to significant differences in their electrochemical performances. There are three noteworthy features in this work: (i) Compared to the previous reported mesocrystal usually comprised of single type of nanoparticle subunit (such as nanospheres, nanorods or nanosheets), hierarchical CuO mesocrystals presented here are made up of nanosheet and nanorod subunits with consistent crystallographically orientation, which is observed for the first time for the hierarchical mesocrystals to the best of our knowledge. (ii) Although great efforts have been made on the synthesis of mesocrystals, and various driving mechanisms, such as surface tension, capillary effects, electrostatic, and steric repulsion etc., are proposed according to the different synthesis systems, the formation mechanism of mesocrystals remains largely uncertain. Herein, we proposed that ionic liquids may present a promising medium for hierarchical mesocrystals by selectively adsorbed in a specific crystal plane of nanoparticle subunits, resulting in their oriented growth with well-defined morphologies in the limited space. (iii) Compared with other counterparts, hierarchical CuO mesocrystals exhibit superior electrochemical properties with good cycling stability and rate capability, which can be attributed to their 3D nanosheet/nanorod superstructures with aligned crystal orientation. It is revealed that 3D hierarchical mesostalline electrodes show an ideal geometry to form stable SEI film by effectively alleviate the volume expansion on the surface of electrode materials. We highly expect these findings are helpful to understand and design hierarchical mesocrystals with distinct structural and geometrical features by the assistance of ionic liquids, thus open up a facile route for maximizing electrochemical activity through morphological control of electrode materials.

2. Experimental Section

Materials: 1-*n*-butyl-3-methylimidazolium chloride ([Bmim]Cl) was obtained from Lanzhou Greenchem ILS, LICP. CAS. China. Other chemicals were purchased from Sigma-Aldrich Company and used without further purification. The water used was deionized.

Preparation of 3D hierarchical CuO mesocrystals: In the typical synthesis procedure, 1.0 mmol of copper chloride ($CuCl_2 \cdot 2H_2O$) and 2.0 mmol of [Bmim]Cl was put into 24 mL of deionized water under stirring to form a homogenous solution. Subsequently, 1 mL of *n*-butylamine was added dropwise into the above homogenous solution under continuous stirring. After stirring for 10 min, the total solution was transferred into a stainless-steel autoclave with a capacity of 33 mL, sealed and heated at 180 ^{o}C for 24 h. When the reaction was completed, the autoclave was cooled to room temperature naturally. The resultant black product was collected and washed with deionized water and anhydrous ethanol for several times until the solution was neutral. The final product was dried in a

vacuum at 60 °C for 6 h. Varying the concentration of [Bmim]Cl could produce CuO nanomaterilas with different morphologies and crystal forms.

Characterization: The products were characterized by XRD, SEM, TEM, HR-TEM, and FT-IR measurements. XRD measurements were performed on a Rigaku D/max 2500 diffractometer with Cu Kα radiation (λ= 0.154056 nm) at V= 40 kV and I = 150 mA, and the scanning speed was 6°/min. Morphology observations were performed on a Hitachi S4800 field emission scanning electron microscope (FE-SEM). TEM and HR-TEM images were recorded with a Tecnai G2 20S-Twin transmission electron microscope operating at an accelerating voltage of 120 kV. The FT-IR spectra of the samples were conducted at room temperature with a KBr pellet on a VECTOR-22 (Bruker) spectrometer ranging from 400 to 4000 cm^{-1}. The pore diameter and the pore size distributions were determined by the Barrett–Joyner–Halenda (BJH) method. The specific surface areas (SBET) of the samples were calculated following the multipoint BET procedure.

Electrochemical Test: Electrochemical studies were characterized in CR2025-type coin cell with a multi-channel current static system Arbin (Arbin Instruments BT 2000, USA). The working electrodes were prepared by a slurry coating method on a copper foil with 80 wt% active materials (CuO), 10 wt% acetylene black, and 10 wt% polyvinylidene fluoride (PVDF) dispersed in *N*-methyl-2-pyrrolidone (NMP). Test cells were assembled in an argon-filled glove box with water and oxygen contents less than 1 ppm using Li foil as the combined reference and counter electrode and polypropylene film (Celgard 2400) as separator. The electrolyte was 1 M $LiPF_6$ in a 1:1 (V/V) mixture of ethylene carbonate (EC) and dimethyl carbonate (DMC). The cells were galvanostatically discharge-charged at a constant current density of 0.1 C (1 C = 670 mA g^{-1}) based on the weight of CuO sample between 0.01 and 3 V at the room temperature. Cyclic voltammetry (CV) was conducted on an electrochemical workstation (CHI660E) at a scan rate of 0.1 mV s^{-1} from 0.01 to 3.0 V. Electrochemical impedance spectroscopy (EIS) was also performed on the electrochemical workstation. The frequency of EIS ranged from 100 kHz to 0.01 Hz at the open-circuit potential.

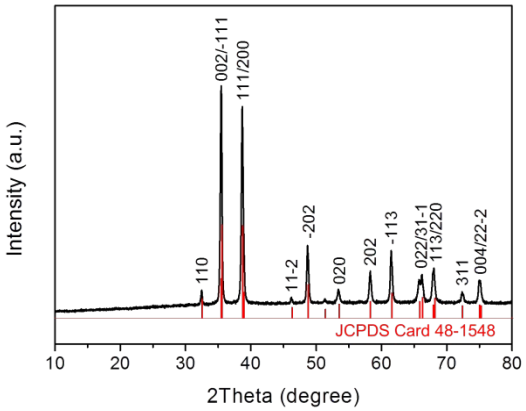

Figure 1. XRD pattern of as-prepared hierarchical CuO mesocrystals.

3. Results and Discussion

3.1. Structures and Morphologies of as-prepared Hierarchical CuO Mesocrystals

The phase and purity of the as-prepared hierarchical CuO mesocrystals were characterized by powder XRD measurements, as shown in **Figure 1**. It is evident that all the diffraction peaks can be perfectly indexed to the monoclinic CuO with lattice constants *a* = 4.6883 Å, *b* = 3.4229 Å, *c* = 5.1319 Å, which are consistent with the reported values (JCPDS Card 48-1548).[38] To further examine the representative morphologies and structures of CuO mesocrystals, scanning electron microscope (SEM) and transmission electron microscope (TEM) were recorded (**Figure 2**). Figure 2A shows a low-magnification SEM image of the as-prepared sample in the presence of ionic liquid precursor, which suggests the large-scale formation of micrometer-sized hierarchical particles predominantly 1.0-1.2 μm in length and 0.8-1.0 μm in width. The hierarchical particles are composed of highly ordered nanosheets with length around 600 nm and width around 400 nm. These nanosheets serve as building blocks and connect together in both horizontal and vertical direction to form the main framework. A high-magnification SEM image shown in Figure 2b reveals the nanosheet subunits' surface is not smooth and apparently built from nanorods with diameters around 10 nm. Repeated 1D growth of these nanorods provide space for higher order organization of CuO mesocrystals, culminating in approximately parallel nanorods exhibiting well-ordered orientation and a low filling factor. Figure 2C shows a typical TEM image of a single CuO mesocrystal, confirming that the hierarchical particle consists of nanosheet and nanorod subunits. The related selected area electron diffraction (SAED) pattern exhibits diffraction spots indexing to [001] zone axis of monoclinic CuO, indicating that the whole hierarchical particle has a single-crystal-like structure (Figure 2D). It suggests that the whole assembly of the nanosheet and nanorod subunits is highly oriented, even though the diffraction spots are slightly elongated, which may be attributed to the small lattice mismatch between the nanosheet and nanorod subunits when they are assembled in the same orientation, typical for mesocrystal.[44] The high-magnification TEM image (Figure 2E) is taken at the junction of the nanosheet and nanorod. From the related fast Fourier transform (FFT) pattern, the diffraction spots are projected by the (200), (020) and (110) planes, and their equivalent planes under an incident electron beam along [001] axis of monoclinic CuO, indicating that the nanosheet subunits are enclosed by (001) planes and the nanorod subunits grow along [010] direction. The corresponding HRTEM image (Figure 2F) can further confirm its single-crystal-like nature. The clear lattice fringe calculated as 0.272 nm can be well assigned to the (110) plane spacing of monoclinic CuO, while atomic defects and planar mismatches in or among the crystallites are visible, in good agreement with the SAED pattern. Both HRTEM and SAED observation suggests the nanosheet and nanorod subunits are well oriented along [010] direction.

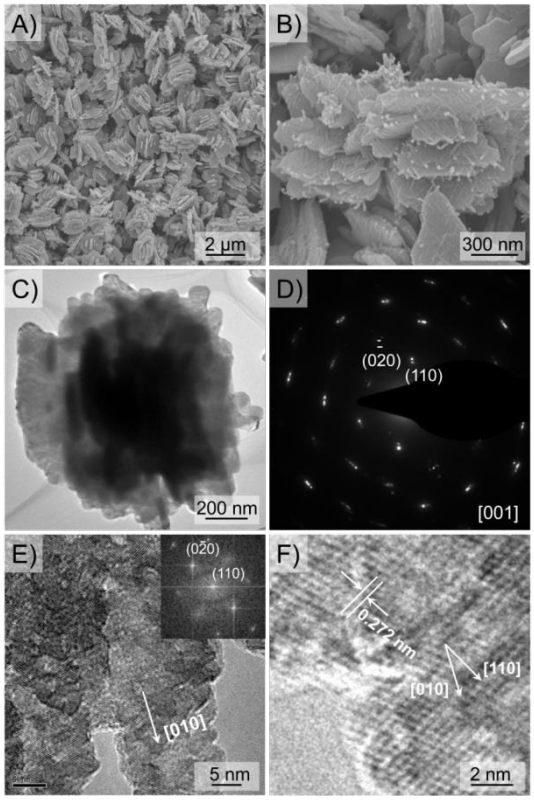

Figure 2. Representative morphologies and structures of as-prepared 3D hierarchical CuO mesocrystals in the presence of 2 mmol [Bmim]Cl: (A) Low- and (B) high-magnification SEM images; (C) Typical TEM image and (D) corresponding SAED pattern viewed along the [001] direction; (E) High-magnification TEM image and corresponding HRTEM image taken from the edge of panel C.

3.2. Effect of [Bmim]Cl on the Formation of CuO with Various Morphologies

For elucidating the role played by [Bmim]Cl on the formation of 3D hierarchical CuO mesocrystals, a series of concentration-dependent experiments were conducted with other experimental conditions remain the same. All of the diffraction peaks in the XRD patterns (Figure S1) of the obtained samples at different [Bmim]Cl concentration can be indexed to the monoclinic CuO (JCPDS Card 48-1548), while their morphologies present significant difference. In the absence of [Bmim]Cl, butterfly-like nanosheets with length around 400 nm and width around 300 nm can be obtained (**Figure 3A** and B). From the corresponding SAED pattern (Figure 3C), it can be seen that the rhombus of diffraction ring can be indexed to the [001] zone axis of monoclinic CuO, suggesting the butterfly-like nanosheet is single crystals and the exposed planes are {001} planes with selectively etching along the *b*-axis. In the previous reports,[58, 59] the *n*-butylamine molecule can form $Cu(CH_3CH_2CH_2CH_2NH_2)_4^{2+}$ by means of nitrogen atom, thus selective adsorption of *n*-butylamine molecules to specific crystal planes of CuO in the growth process may play an important role on the formation of CuO nanosheets with {001} dominant exposed planes. For monoclinic CuO, the {010} planes have the lowest surface energy (1.04 J m^{-2}), followed by the {100} planes (1.73 J m^{-2}), and the {001} planes have the largest surface energy (4.23 J m^{-2}).[31] In order to minimize the energy of the reaction system, *n*-butylamine molecules could selectively passivate the {001} planes and hider the growth of monoclinic CuO crystal along <001> direction, leading the formation of {001} plane dominant nanosheets according to Cornell and Schwertmann.[59] In contrast, the {010} planes, where *n*-butylamine molecules are adsorbed more sparsely, are more easily to be etched in the vigorous hydrothermal reaction at high temperature. The preferential etching occurs along the [010] direction since the {010} planes are lack of effective protection, resulting in the formation of butterfly-like nanosheets exposed {001} planes with etching along the *b*-axis.

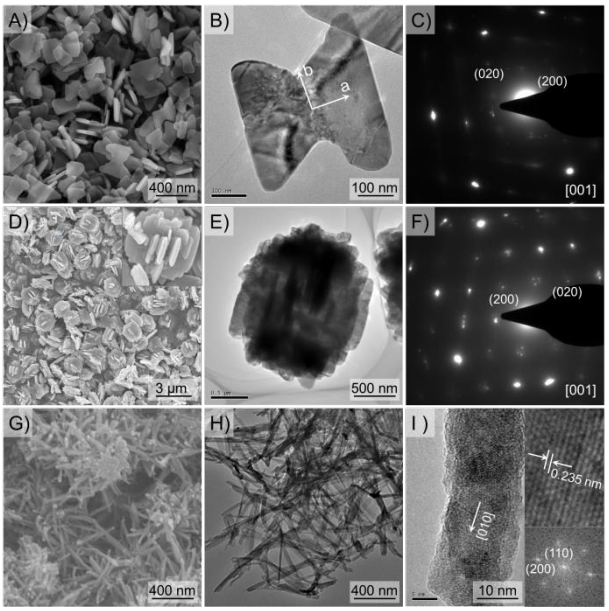

Figure 3. SEM images and corresponding TEM images and SAED patterns of CuO nanostructures with different morphologies at different concentrations of [Bmim]Cl: (A-C) 0 mmol, butterfly-like nanosheets; (D-F) 1 mmol, hierarchical mesocrystals composed of nanosheets; (G-I) 5 mmol, nanorods.

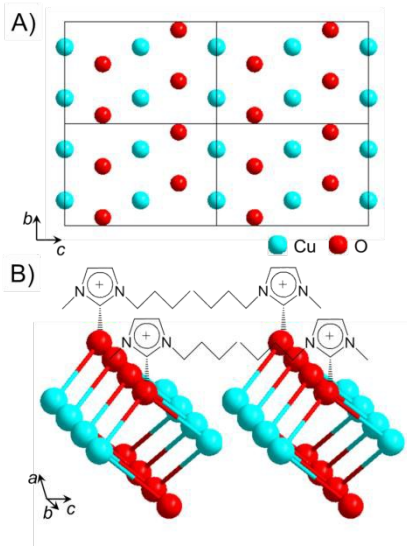

Figure 4. (A) Structure illustration of monoclinic CuO viewed along [100] direction (4 × 4× 4 cells); (B) Scheme for $[Bmim]^+$ ions perpendicular to the {100} planes of CuO and self-assemble into ordered structures along [010] direction.

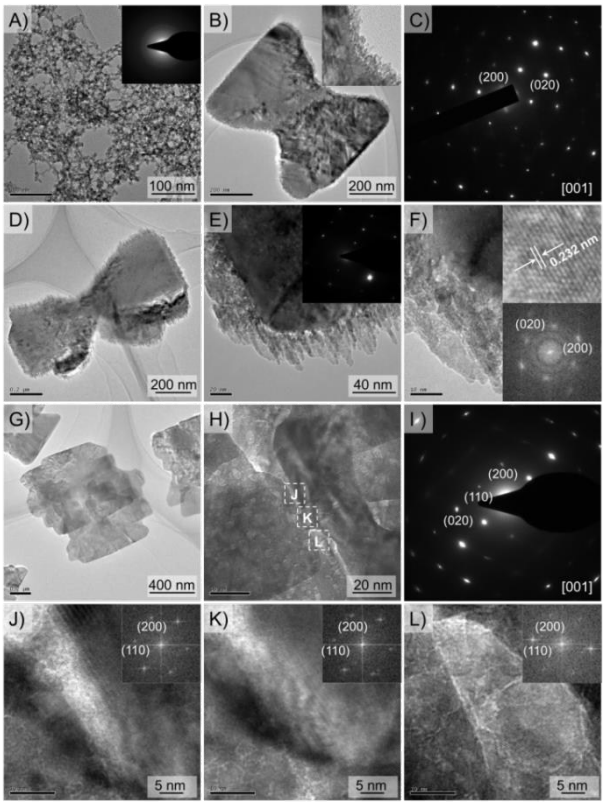

Figure 5. Typical TEM images and corresponding SAED patterns of hierarchical CuO mesocrystals obtained at different reaction times: (A) 0.5 h, amorphous precursor particles; (B and C) 2 h, primary nanosheet; (D-F) 4 h, primary particle composed of nanosheet and nanorod subunit; (G-L) 12 h, mesocrystal intermediate.

When introducing ionic liquid ([Bmim]Cl) into the reaction system, remarkable transition from butterfly-like nanosheets to hierarchical mesocrystals composed of nanosheet and nanorod subunit was occurred (Figure 2), thus an important conclusion can be drawn: the existence of [Bmim]Cl must be the key to induce the nanosheet and nanorod subunits to orient along [010] direction. Different from typical molecular (*n*-butylamine in the present case), [Bmim]Cl has highly ionic nature, which can interact with nanoparticles to facilitate a remarkably well defined layer structure in the vicinity of a solid-liquid boundary. In the research reported here, $[Bmim]^+$ ions can be preferred to adsorb on the O^{2-}-terminated {100} surface of CuO nanoparticles by electrostatic force. More importantly, the hydrogen bond can be induced to form between the hydrogen atom at C2 position of the imidazole ring and the bridged oxygen atoms of {100} planes along [010] direction. According to the previous report,[60-74] $[Bdmim]^+$ ions have very strong tendency to self-assemble into ordered structures stabilized by additional π–π interactions along the aligned hydrogen bonds, which is very conducive to form self-assembly superstructure. Based on the above analysis, $[Bmim]^+$ ions could interact strongly with the {100} planes and align perpendicular to the CuO particles, thus promoted the preferential growth of CuO nanoparticle subunits along [010] direction (**Figure 4**), leading the formation of hierarchial CuO mesocrystals composed of nanosheet subunits (Figure 3D-F) or nanosheet and nanorod subunits (Figure 2) depended on the concentration of [Bmim]Cl. To shed light on the adsorption of $[Bmim]^+$ ions on the CuO surfaces, FT-IR spectra of the as-prepared CuO mesocrystals were measured, which were shown in Figure S2. When $[Bmim]^+$ ions are immobilized on to CuO mesocrystals, the peaks of imidazole ring stretching vibration aroud 3500 cm^{-1} are shifted to lower wavenumbers due to less electron density by means of polarization via hydrogen bonding according to previous reports, indicating a strong interaction between $[Bmim]^+$ ions and CuO surface.

When increased the amount of [Bmim]Cl to 5 mmol, CuO rod-like single-crystals were obtained (Figure 3G-I), which can be attributed to the enhancement of stabilizing the {100} planes of CuO nanoparticles in the high concentration of ionic liquid. Figure 3G shows a low-magnification SEM, which indicates the as-prepared sample is well-shaped nanorods with a diameter of 20 nm. From the TEM and HRTEM images, it can be seen the clear lattice fringes and the interplane distance is calculated as 0.235 nm, corresponding to the (100) crystal planes of monoclinic CuO. The diffraction spots in related FFT pattern can be indexed to {200}, {020} and {110} planes, indicating that the obtained CuO nanorod exhibited a preferred growth orientation along the [010] direction.

3.3. Possible Growth Mechanism of Hierarchical CuO Mesocrystals from Ionic Liquid Precursor

To shed light on the formation of hierarchical CuO mesocrystals, a time-dependent experiment was carried out. As shown in **Figure 5A**, colloidal nanoparticles were the domain product after 0.5 h, the corresponding SAED pattern suggested their amorphous nature. No obvious diffraction peaks are observed in the XRD pattern (Figure S3a), further confirmed the colloidal nanoparticles adopt amorphous phase. This is understandable in the initial reaction stage, the hydrolysis of Cu^{2+} is very weak due to complexation of *n*-butylamine and [Bmim]Cl, resulting in a high degree of supersaturation. According to the Ostwald rule of stages: the least sable and least dense modification also has the lowest activation barrier of formation, thus amorphous particles are favored to form as the initial species at high supersaturation.[3] Subsequently, transformation reactions occurred (Figure S3b-d). When the reaction time was further increased to 2-4 h, butterfly-like nanosheets first appeared due to the protection of {001} planes by *n*-butylamine molecule and etch of {010} planes by hydrolysis reaction. Under vigorous hydrothermal reaction at high temperature, there was large number of dangling bonds present in the {010} planes, thus the second order of primary particles tended to grow along [010] direction induced by [Bmim]Cl. The related HRTEM and corresponding FFT pattern suggest those subunits actually adopted a single-crystal-like mesoscopic structure (Figure 5B and C). Due to the high interface energy between {010} planes, those second order of primary particles were prone to high colloidal attraction, where bonding between the particles allows the system to win a substantial amount of energy by eliminating two high-energy planes by crystallographic fusion, towards apparent nanorods along [010] direction (Figure 5D-F). Due to high ionic nature, [Bmim]Cl can interact with those primary

particles to facilitate a self-assembly superstructure by π–π interactions along the aligned hydrogen bonds, leading to the formation of 3D framework structure of primary particles composed of nanosheet and nanorod subunits by vertical attachment (Figure 5G). The next growth process involves the competition between van der Waals forces favoring the vertical growth and uncompensated dangling bonds forcing the nanorods to grow laterally on the surface of nanosheets. Those primary particles attach to each other through a common crystallographic face, creating fully formed stable 3D mesocrystals through a nonclassical crystal growth mechanism. The corresponding TEM images and SAED pattern suggest the 3D mesocrystals composed of nanosheet and nanorod subunit display single-crystal-like mesoscopic structure exposed {001} planes (Figure 5H and I). In particular, Figure 5J-L show the representative high magnification TEM image of the circled area in Figure 5H, providing the adjacent primary particle adopts the consistent crystallographic orientation by oriented attachment. Overall, based on the previous analysis, our proposed reaction mechanism in **Figure 6** is able to explain successfully the formation of 3D hierarchical CuO mesocrystal with prolonged reaction time.

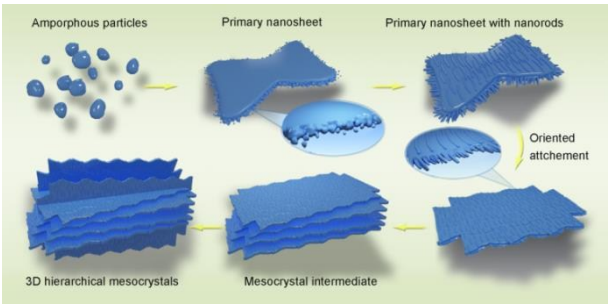

Figure 6. Schematic illustration of shape evolution of 3D hierarchical CuO mesocrystals.

3.4. Electrochemical Performance of CuO with Various Morphologies and Crystal Forms

There is much recent interest in mesocrystals as electrode materials for Li-ion batteries due to their inherent and uniform porosity associated with well-defined nanoparticle orientation. Since the 3D hierarchical CuO mesocrystals (CuO-HM) are constructed by nanosheet and nanorod subunits, they may be expected to exhibit superior electrochemical property compared with normal CuO crystals. To this end, their electrochemical behaviors as anode materials for Li-ion batteries were explored. For comparison, the performances of CuO nanosheets (CuO-NS) and CuO nanorods (CuO-NR) were also investigated. Cyclic voltammetry (CV) was employed to understand the electrochemical reactive processes of 3D hierarchical CuO mesocrystals. **Figure 7A** depicts the CV curves of 3D hierarchical CuO mesocrystals in the range of 0.01-3 V at a scan rate of 0.1 mV s^{-1}. During the first discharging process, it is found that there are three reduction peaks located at 1.65, 0.93 and 0.62 V, corresponding to multi-step electrochemical reactions that involve the intermediate copper oxide phase ($Cu_{1-x}^{II}Cu_x^{I}O_{1-x/2}$), the formation of Cu_2O phase, and the decomposition of Cu_2O into Cu and Li_2O, respectively. Subsequently, during the charging process, two oxidation peaks located at about 1.43 and 2.36V can be assigned to the formation of Cu_2O and the oxidation of Cu_2O to CuO, respectively. In the subsequent cycles, the CV curves are very similar in shape expect the reduction peaks shift to higher potentials, while the oxidation peaks stay almost at the same locations. Figure 7B presents the rate capability of the CuO electrodes with different morphologies and crystal forms from 67 to 670 mA g^{-1} for ten cycles at each current rate. It is revealed that the 3D hierarchical CuO mesocrystals retained good rate capability as the current density increased by 10 times. After 50 cycles, the 3D hierarchical CuO mesocrystal electrode can still deliver a high specific capacity of nearly 350 mAh g^{-1}, which is much higher than the CuO nanosheet electrode (170 mAh g^{-1}) and nanorod electrode (130 mAh g^{-1}).

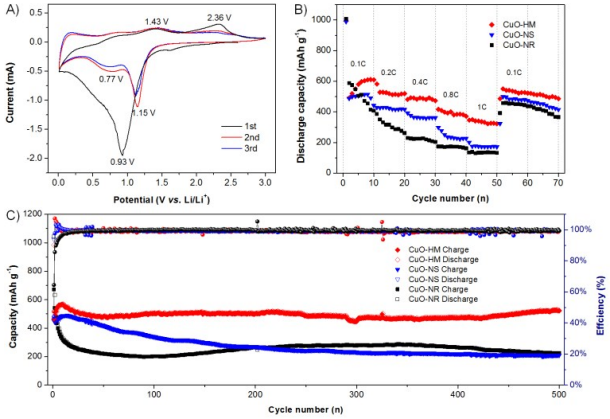

Figure 7. (A) CV curves of hierarchical CuO mesocrystals obtained at a scanning rate of 0.1 mV s^{-1}; (B) Rate capabilities and (C) cycling performance of hierarchical CuO mesocrystals, CuO nanosheets, and CuO nanorods.

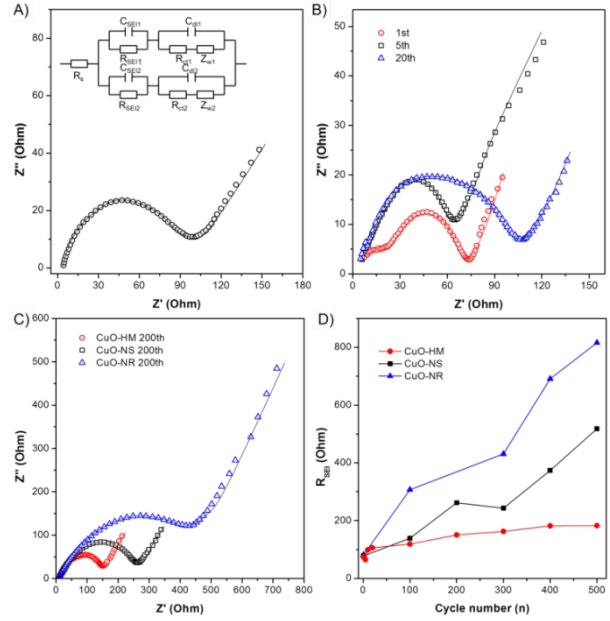

Figure 8. Nyquist polts of CuO electrodes at different cycle performance: (A) 10th, (B) 1st, 5th and 20th for hierarchical CuO mesocrystals; (C) 200th for hierarchical CuO mesocrystals, CuO nanosheets, and CuO nanorods. The inset in (A) describes the equivalent circuit model. Symbols and lines indicate experimental and calculated data,

respectively. (D) The fitted R_{SEI} results of CuO electrodes with different morphologies at different cycles.

Another outstanding feature of the 3D hierarchical CuO mesocrystalline electrode is the cycling performance. Taking into account the molar volume of initial CuO electrode and fully theoretical lithiation phase (CuO converts to Cu and Li_2O), the volume change during Li uptake can be calculated to be around 80%, which will lead to the pulverization problem and unstable SEI formation, and moreover a rapid deterioration in capacity, limiting the lifetime of CuO electrodes for Li-ion batteries. Interestingly, the 3D hierarchical CuO mesocrystalline electrodes exhibited an excellent stable cycling performance investigated by the galvanostatic charge and discharge method between 0.01 and 3.0 V at a current density of 67 mA g^{-1}. The reversible capacity of 3D hierarchical CuO mesocrystalline electrode after 500 cycles was 525.2 mAh g^{-1}. For the counterparts, only 210.1 and 224.7 mAh g^{-1} were maintained in the CuO nanosheets and nanorods, respectively (Figure 7C). The superior cycling performance for 3D hierarchical CuO mesocrystals can be attributed to three factors: (i) the unique self-assembled hierarchical structure with low filling factor may contribute to the improved electrochemical performance towards lithium storage, while the microscopic structure assembled by nanosheets guarantees the integrity of particles as well as quick infiltration of electrolyte. The oriented self-assembly of nanorods on the nanosheet matrix surface may ensure that most CuO building blocks participate in the electrochemical reactions and thus provide large electrode/electrolyte contact areas, leading to a short diffusion length and an enhanced electronic conductivity necessary for high capacity; (ii) hierarchical CuO mesocrystal composed of nanosheet and nanorod subunits with intracrystalline porosity provides extra space to mitigate volume expansion and extraction, which can act as a buffering layer to alleviate the adverse effect of lattice distortion experienced during Li uptake/release process. The nitrogen isothermal adsorption measurement was carried out to evaluate the porous structure and the BET surface area. The N_2 adsorption/desorption isothermal and the adsorption pore size distribution plot of as-prepared 3D hierarchical CuO mesocrystals can be observed in Figure S6. It can be seen that the sample displays a type IV isotherm with a typical H3 hysteresis loop ($0.5<P/P_0<1$), which suggests its mesoporous feature. The pore-size distribution (inset) further confirmed the mesoporous characterization of the 3D hierarchical CuO mesocrystals;[75] (iii) hierarchical mesocrystals assembled by nanosized subunits may show an ideal geometry for battery electrodes due to significantly less formation of SEI film on the surface as compared with large surface area nanostructures. Although nanostructured electrodes can mitigate the volume expansion by enhancement of Li-ion diffusion, relaxation of inner lattice stress and reduction of electrode exfoliation, they still suffer capacity degradation on prolonged cycling primarily due to unstable SEI film. The repetitive volume expansion/contraction during cycling can fracture the SEI film, exposing new active surface for SEI film growth, thus a thicker SEI film can form, which will consume electrolytes and lithium ions, reduce electrical conductivity and retard Li-ion diffusion, degrading battery performance tremendously. In comparison, 3D hierarchical CuO mesocrystal composed of nanosheet and nanorod subunits with intracrystalline porosity can provide large free volume inside, offering a more favourable way for the inward volume change during full lithiation process, and it may gradually convert back to the original structure during delithiation process. Thus, hierarchical mesocrystalline electrodes present more robust against repetitive volume changes, and the SEI film on surface is more stable due to harmless against mechanical stress induced by volume changes, leading to long-lived and stable cycling performance.

Electrochemical impedance spectroscopy (EIS) measurements were performed to probe the effect of hierarchical mesocrystalline structure on the cycling performance of cells and to understand the electrochemical process occurring in the electrode/electrolyte interface in the Li-ion batteries.[76-80] Taking account into the 3D hierarchical CuO mesocrystals are constituted by the anisotropic subunits, the diffusion route of Li^+ ions must be different from the isotropic particles. For the sheet-shaped structure exposed {001} planes, the diffusion length through [001] direction is obviously shorter than the [100] and [010] direction. Besides, the {001} planes yield lower interaction energy of lithium (1.88 J m^{-2}) than {100} planes (6.05 J m^{-2}) and {010} planes (8.47 J m^{-2}) due to their high surface energy, which can provide more reactive sites to facilitate interaction with Li^+ ions.[31] In the previous work, Aurbach et al. have employed a two-parallel diffusion path model to perfectly describe the kinetics of slab-shaped particles and nonhomogenous composite electrode.[81] Inspired by this, a modified two-parallel diffusion path model is set up, and the corresponding equivalent circuit is presented in **Figure 8A**.[82] According to the equivalent circuit, the EIS consisted of two partially overlapped and depressed semicircles at high-to-middle frequencies and a sloping line at low frequencies. The intercept of the spectrum with the real axis at high frequency referred to the ohmic series resistances (R_s), reflecting the combined resistance of electrolyte, separator and electrode. The depressed semicircle from the high to intermediate frequency was related to the resistance for Li^+ ion migration through the SEI layer (R_{SEI}) and constant phase elements (C_{SEI}) of the SEI layer. The semicircle from intermediate to low frequency was associated with the charge transfer resistance (R_{ct}) and constant phase elements (*CPE*) of the electrode. C_{SEI} and *CPE* were used to take into account the roughness of the CuO electrode surface. The sloping line at low frequency corresponded to the Warburg impedance (Z_w), which was related to the Li^+ ion diffusion within the electrodes. Considering that the hierarchical CuO mesocrystals consists of nanosheet and nanorod subunits with intracrystalline porosity, it requires the activation process to form stable SEI film in the initial cycles. After ten cycles, the reversible capacity is 541 mAh g^{-1}, sustaining 81% of the theoretic capacity. Thus, it is approximately considered that the electrode reaction during the tenth cycle is complete. The tenth cycle simulated data from the equivalent circuit by Z-view software is displayed in

Figure 8A. The excellent fitness between the simulated curve and experimental Nyquist plot indicates the accuracy of the two-parallel diffusion path model. During the first few cycles, the value of R_{SEI} is vibrated and shows a total trend of increasing, which indicates the repetitive decomposition and formation of SEI film (Figure 8B). After ten cycles, the value of R_{SEI} remains almost changeless, indicating an integrated and stable SEI film formed on the surface of hierarchical CuO mesocrystals. However, for the CuO nanosheets and CuO nanorods, the R_{SEI} value increases rapidly with prolong cycles (Figure 8C and D). This contradistinction confirms the hierarchical mesocrystlline structure can lead to the formation of stable SEI film, which is beneficial for the cycling stability of the electrodes.

Conclusions

In summary, 3D hierarchical CuO mesocrystals have been successfully fabricated through a facile ionic liquid-assisted hydrothermal route. The obtained mesocrystals are comprised of highly oriented nanosheet and nanorod subunits and possess a distinct 3D hierarchical superstructure exposed {001} crystal planes. The experimental evidence from time-dependent characterization and isolation of various mesocrystal intermediates suggests that the 3D hierarchical CuO mesocrystals are formed by means of particle-mediated aggregation under high degree of supersaturation, undergoing a mesoscale transformation from amorphous particles to primary nanosheets, and finally to the 3D framework structure composed of nanosheet and nanorod subunits by oriented attachment. Ionic liquid plays an essential role in the non-classical particle mediated aggregation by promoting the primary particles self-assemble along the [010] direction. Due to the inherent porosity associated with well-defined nanoparticle orientation, 3D hierarchical CuO mesocrystals exhibit excellent cycling performance as anode for Li-ion battery over the constituent counterparts, attaining a reversible capacity of 525.2 mAh g^{-1} after 500 cycles at a current density of 67 mA g^{-1}. The superior cycling performance of CuO mesocrystal can be attributed its highly ordered micro-/nano-structure, which favors the formation of stable SEI film during the cycling process. By employing a modified two-parallel diffusion path model, EIS measurements demonstrates the formation of SEI film is greatly influenced by the electrode morphology during cycling. For 3D hierarchical CuO mesocrystals, the value of R_{SEI} remains almost changeless after 10 cycles, indicating an integrated and stable SEI film formed on the surface of hierarchical CuO mesocrystals. For the CuO nanosheets and CuO nanorods, the R_{SEI} value increases rapidly with prolong cycles. The 3D hierarchial CuO mesocrystals developed in the current work not only provide an excellent model to study the 3D self-organization of two types of primary particles, but also open up a facile route for designing mesocrystal-based electrodes for long life Li-ion batteries.

Acknowledgements

This study was supported by the China Postdoctoral Science Foundation (project no. 2014M560531 and 2015T80679), the National Natural Science Foundation of China (grant no. 61574118), and the Key Project of Science and Technology Plan of Fujian Province (grant no.2015H0038).

Notes and references

1 H. Cölfen, M. Antonietti, *Angew. Chem. Int. Edit.* **2005**, *44*, 5576-5591.
2 Y. Liu, Y. Zhang, J. Wang, *CrystEngComm,* **2014,** 16, 5948-5967.
3 H. Cöelfen, M. Antonietti, *Mesocrystals and nonclassical crystallization*, John Wiley & Sons, **2008**.
4 L. Bergström, E. V. Sturm, G. Salazar-Alvarez, H. Cölfen, *Accounts. Chem. Res.* **2015**.
5 M.-G. Ma, H. Cölfen, *Curr. Opin. Colloid Interface Sci.* **2014**, *19*, 56-65.
6 T. Tachikawa, T. Majima, *NPG Asia Mater.* **2014**, *6*, e100.
7 J. Fang, B. Ding, H. Gleiter, *Chem. Soc. Rev.* **2011**, *40*, 5347-5360.
8 L. Zhou, P. O'Brien, *Small* **2008**, *4*, 1566-1574.
9 M. Niederberger, H. Cölfen, *Phys. Chem. Chem. Phys.* **2006**, *8*, 3271-3287.
10 S. J. Yang, M. Antonietti, N. Fechler, *J. Am. Chem. Soc.* **2015**, *137*, 8269-8273.
11 S. Deng, V. Tjoa, H. M. Fan, H. R. Tan, D. C. Sayle, M. Olivo, S. Mhaisalkar, J. Wei, C. H. Sow, *J. Am. Chem. Soc.* **2012**, *134*, 4905-4917.
12 P. Tartaj, J. M. Amarilla, *Adv. Mater.* **2011**, *23*, 4904-4907.
13 L. Zhou, D. Smyth-Boyle, P. O'Brien, *J. Am. Chem. Soc.* **2008**, *130*, 1309-1320.
14 X. Fei, W. Li, Z. Shao, S. Seeger, D. Zhao, X. Chen, *J. Am. Chem. Soc.* **2014**, *136*, 15781-15786.
15 Y.-Y. Kim, A. S. Schenk, J. Ihli, A. N. Kulak, N. B. Hetherington, C. C. Tang, W. W. Schmahl, E. Griesshaber, G. Hyett, F. C. Meldrum, *Nature Commun.* **2014**, *5*.
16 S. Liu, J. Zhang, W. Tu, J. Bao, Z. Dai, *Nanoscale* **2014**, *6*, 2419-2425.
17 J. Ihli, P. Bots, A. Kulak, L. G. Benning, F. C. Meldrum, *Adv. Funct. Mater.* **2013**, *23*, 1965-1973.
18 Y. Zhao, Y. Lu, Y. Hu, J. P. Li, L. Dong, L. N. Lin, S. H. Yu, *Small* **2010**, *6*, 2436-2442.
19 Z. Liu, X. Wen, X. Wu, Y. Gao, H. Chen, J. Zhu, P. Chu, *J. Am. Chem. Soc.* **2009**, *131*, 9405-9412.
20 T. Wang, H. Cölfen, M. Antonietti, *J. Am. Chem. Soc.* **2005**, *127*, 3246-3247.
21 X. Duan, S. Xiao, L. Wang, H. Huang, Y. Liu, Q. Li, T. Wang, *Nanoscale* **2015**, *7*, 2230-2234.
22 X. Duan, J. Ma, J. Lian, W. Zheng, *CrystEngComm* **2014**, *16*, 2550-2559.
23 J. Ma, J. Teo, L. Mei, Z. Zhong, Q. Li, T. Wang, X. Duan, J. Lian, W. Zheng, *J. Mater. Chem.* **2012**, *22*, 11694-11700.
24 Z. Ma, J. Yu, S. Dai, *Adv. Mater.* **2010**, *22*, 261-285.
25 T. Y. Kim, W. J. Kim, S. H. Hong, J. E. Kim, K. S. Suh, *Angewandte Chemie* **2009**, *121*, 3864-3867.
26 A. Taubert, A. Uhlmann, A. Hedderich, K. Kirchhoff, *Inorg. Chem.* **2008**, *47*, 10758-10764.
27 Z. Li, A. Geßner, J. P. Richters, J. Kalden, T. Voss, C. Kübel, A. Taubert, *Adv. Mater.* **2008**, *20*, 1279-1285.
28 Z. Li, A. Shkilnyy, A. Taubert, *Crystal Growth and Design* **2008**, *8*, 4526-4532.
29 M. Antonietti, D. Kuang, B. Smarsly, Y. Zhou, *Angew. Chem. Int. Edit.* **2004**, *43*, 4988-4992.
30 Z. Bai, Y. Zhang, Y. Zhang, C. Guo, B. Tang, *Electrochim. Acta* **2015**, *159*, 29-34.

31 D. Su, X. Xie, S. Dou, G. Wang, *Scientific Reports* **2014**, *4*.
32 X. Zhang, J. Zhou, H. Song, X. Chen, Y. V. Fedoseeva, A. V. Okotrub, L. G. Bulusheva, *Acs Appl. Mater. Interfaces* **2014**, *6*, 17236-17244.
33 C. Wang, D. Higgins, F. Wang, D. Li, R. Liu, G. Xia, N. Li, Q. Li, H. Xu, G. Wu, *Nano Energy* **2014**, *9*, 334-344.
34 C. Wang, Q. Li, F. Wang, G. Xia, R. Liu, D. Li, N. Li, J. S. Spendelow, G. Wu, *Acs Appl. Mater. Interfaces* **2014**, *6*, 1243-1250.
35 A. Banerjee, U. Singh, V. Aravindan, M. Srinivasan, S. Ogale, *Nano Energy* **2013**, *2*, 1158-1163.
36 M. Reddy, G. Subba Rao, B. Chowdari, *Chem. Rev.* **2013**, *113*, 5364-5457.
37 M. Reddy, C. Yu, F. Jiahuan, K. P. Loh, B. Chowdari, *Acs Appl. Mater. Interfaces* **2013**, *5*, 4361-4366.
38 O. Waser, M. Hess, A. Güntner, P. Novák, S. E. Pratsinis, *J. Power Sources* **2013**, *241*, 415-422.
39 L. Wang, W. Cheng, H. Gong, C. Wang, D. Wang, K. Tang, Y. Qian, *J. Mater. Chem.* **2012**, *22*, 11297-11302.
40 J. Wang, Y. Liu, S. Wang, X. Guo, Y. Liu, *J. Mater. Chem. A,* **2014,** 2, 1224-1229.
41 R. Wu, X. Qian, F. Yu, H. Liu, K. Zhou, J. Wei, Y. Huang, *J. Mater. Chem. A,* **2013,** 1, 11126-11129.
42 J. M. Amarilla, E. Morales, J. Sanz, I. Sobrados, P. Tartaj, *J. Power Sources* **2015**, *273*, 368-374.
43 T. Lan, H. Qiu, F. Xie, J. Yang, M. Wei, *Scientific reports* **2015**, *5*.
44 D. Su, S. Dou, G. Wang, *Nano Research* **2014**, *7*, 794-803.
45 R. Jin, J. Zhou, Y. Guan, H. Liu, G. Chen, *Journal of Materials Chemistry A* **2014**, *2*, 13241-13244.
46 Y. Liu, J. Bai, X. Ma, J. Li, S. Xiong, *Journal of Materials Chemistry A* **2014**, *2*, 14236-14244.
47 E. Uchaker, G. Cao, *Nano Today* **2014**, *9*, 499-524.
48 Q. Li, L. Yin, Z. Li, X. Wang, Y. Qi, J. Ma, *Acs Appl. Mater. Interfaces* **2013**, *5*, 10975-10984.
49 N. Zhou, H.-Y. Wang, E. Uchaker, M. Zhang, S.-Q. Liu, Y.-N. Liu, G. Cao, *J. Power Sources* **2013**, *239*, 103-110.
50 F. Dang, T. Hoshino, Y. Oaki, E. Hosono, H. Zhou, H. Imai, *Nanoscale* **2013**, *5*, 2352-2357.
51 E. Uchaker, M. Gu, N. Zhou, Y. Li, C. Wang, G. Cao, *Small* **2013**, *9*, 3880-3886.
52 Y. Chen, B. Qu, L. Mei, D. Lei, L. Chen, Q. Li, T. Wang, *J. Mater. Chem.* **2012**, *22*, 25373-25379.
53 X. Duan, L. Mei, J. Ma, Q. Li, T. Wang, W. Zheng, *Chem. Commun.* **2012**, *48*, 12204-12206.
54 Z. Hong, M. Wei, T. Lan, G. Cao, *Nano Energy* **2012**, *1*, 466-471.
55 Z. Hong, M. Wei, T. Lan, L. Jiang, G. Cao, *Energy & Environmental Science* **2012**, *5*, 5408-5413.
56 J. Popovic, R. Demir‐Cakan, J. Tornow, M. Morcrette, D. S. Su, R. Schlögl, M. Antonietti, M. M. Titirici, *Small* **2011**, *7*, 1127-1135.
57 J. Ye, W. Liu, J. Cai, S. Chen, X. Zhao, H. Zhou, L. Qi, *J. Am. Chem. Soc.* **2010**, *133*, 933-940.
58 Y. Li, B. Tan, Y. Wu, *Chem. Mater.* **2007**, *20*, 567-576.
59 Z.-p. Zhang, H.-p. Sun, X.-q. Shao, D. Li, H. Yu, M. Han, *Adv. Mater.* **2005**, *17*, 42-47.
60 X. Duan, S. Xiao, Y. Liu, H. Huang, D. Wang, L. Wang, B. Liu, T. Wang, *Nanotechnology* **2015**, *26*, 031001.
61 G. Zhou, X. Duan, B. Liu, Q. Li, T. Wang, *Nanoscale* **2014**, *6*, 11041-11045.
62 X. Duan, T. Kim, D. Li, J. Ma, W. Zheng, *Chem.-Eur. J.* **2013**, *19*, 5924-5937.
63 X. Duan, D. Li, H. Zhang, J. Ma, W. Zheng, *Chem.-Eur. J.* **2013**, *19*, 7231-7242.
64 D. Freudenmann, S. Wolf, M. Wolff, C. Feldmann, *Angewandte Chemie International Edition* **2011**, *50*, 11050-11060.
65 J. Le Bideau, L. Viau, A. Vioux, *Chem. Soc. Rev.* **2011**, *40*, 907-925.
66 X. Zhao, W. Jin, J. Cai, J. Ye, Z. Li, Y. Ma, J. Xie, L. Qi, *Adv. Funct. Mater.* **2011**, *21*, 3554-3563.
67 X. Duan, J. Lian, J. Ma, T. Kim, W. Zheng, *Crystal Growth & Design* **2010**, *10*, 4449-4455.
68 T. Torimoto, T. Tsuda, K. i. Okazaki, S. Kuwabata, *Adv. Mater.* **2010**, *22*, 1196-1221.
69 N. Recham, L. Dupont, M. Courty, K. Djellab, D. Larcher, M. Armand, J.-M. Tarascon, *Chem. Mater.* **2009**, *21*, 1096-1107.
70 J. S. Lee, X. Wang, H. Luo, G. A. Baker, S. Dai, *J. Am. Chem. Soc.* **2009**, *131*, 4596-4597.
71 H. S. Park, B. G. Choi, S. H. Yang, W. H. Shin, J. K. Kang, D. Jung, W. H. Hong, *Small* **2009**, *5*, 1754-1760.
72 H. Weingärtner, *Angewandte Chemie International Edition* **2008**, *47*, 654-670.
73 W. Zheng, X. Liu, Z. Yan, L. Zhu, *ACS nano* **2008**, *3*, 115-122.
74 Y. Zhou, J. H. Schattka, M. Antonietti, *Nano Lett.* **2004**, *4*, 477-481.
75 X. Duan, J. Yang, H. Gao, J. Ma, L. Jiao, W. Zheng, *CrystEngComm,* **2012,** 14, 4196-4204.
76 J. Guo, A. Sun, X. Chen, C. Wang, A. Manivannan, *Electrochim. Acta* **2011**, *56*, 3981-3987.
77 T. Hang, D. Mukoyama, H. Nara, N. Takami, T. Momma, T. Osaka, *J. Power Sources* **2013**, *222*, 442-447.
78 T. Hang, D. Mukoyama, H. Nara, T. Yokoshima, T. Momma, M. Li, T. Osaka, *J. Power Sources* **2014**, *256*, 226-232.
79 O. S. Mendoza-Hernandez, H. Ishikawa, Y. Nishikawa, Y. Maruyama, Y. Sone, M. Umeda, *Electrochim. Acta* **2014**, *131*, 168-173.
80 H. Zhou, M.-A. Einarsrud, F. Vullum-Bruer, *J. Power Sources* **2013**, *238*, 478-484.
81 M. Levi, D. Aurbach, *The Journal of Physical Chemistry B* **2004**, *108*, 11693-11703.
82 J. Xiang, J. Tu, Y. Qiao, X. Wang, J. Zhong, D. Zhang, C. Gu, *The Journal of Physical Chemistry C* **2011**, *115*, 2505-2513…

Graphical Abstract

3D hierarchical CuO mesocrystals have been prepared from ionic liquid precursor under hydrothermal conditions, and exhibit superior electrochemical performance as anode materials. The unique characteristics of hierarchical mesostalline electrodes show an ideal geometry to form stable SEI film, which offers a facile route in designing high-performance electrodes for long-lived Li-ion batteries.